

Iterative multiple reference tissue method for estimating pharmacokinetic parameters on prostate DCE MRI

Shoshana B. Ginsburg^a, B. Nicolas Bloch^b, Neil M. Rofsky^c, Elizabeth M. Genega^d, Robert E. Lenkinski^c, and Anant Madabhushi^a

^aCase Western Reserve University, Cleveland, Ohio; ^bBoston University School of Medicine, Boston, Massachusetts; ^cUT Southwestern Medical Center, Dallas, Texas; ^dBeth Israel Deaconess Medical Center, Boston, Massachusetts

ABSTRACT

Pharmacokinetic (PK) parameters are probes of tissue status that can be assessed by analysis of dynamic contrast-enhanced (DCE) MRI and are useful for prostate cancer (CaP) detection and grading. Traditionally, PK analysis requires knowledge of the time-resolved concentration of the contrast agent in the blood plasma, the arterial input function (AIF), which is typically estimated in an artery in the field-of-view (FOV). In cases when no suitable artery is present in the FOV, the multiple reference tissue method (MRTM) enables the estimation of PK parameters without the AIF by leveraging PK parameter values from the literature for a reference tissue in the FOV. Nevertheless, PK parameters estimated in the prostate vary significantly between patients. Consequently, population-based values obtained from the literature may introduce error into PK parameter estimation via MRTM. The objectives of this paper are two-fold. First we present a novel scheme, iterative MRTM (IMRTM), to estimate PK parameter values in the absence of the AIF without making assumptions about the PK constants associated with a reference tissue. Then, using IMRTM we investigate differences in PK constants between CaP in the peripheral zone (PZ) and CaP in the central gland (CG), as CG and PZ CaP have previously been shown to differ significantly in terms of both texture and prognosis. We apply IMRTM to 15 patients with CaP in either the CG or the PZ who were scheduled for a radical prostatectomy and a pre-operative MRI. Values for the PK parameters K^{trans} and v_e estimated via IMRTM average 0.29 and 0.60 for normal central gland (CG), 0.29 and 0.64 for normal peripheral zone (PZ), and 0.30 and 0.53 for CaP. It is noteworthy that PK constants estimated in PZ CaP are significantly higher than those estimated in CG CaP ($p < 0.05$). While both MRTM and IMRTM provide PK parameter values that are biologically feasible, IMRTM has the advantage that it invokes patient-specific information rather than relying on population-based PK constants in performing PK analysis.

Keywords: Pharmacokinetics, DCE MRI, reference region model, prostate cancer, computer-aided diagnosis

1. INTRODUCTION

Prostate cancer (CaP) is the second leading cause of death in men, and its rate of incidence has increased in recent years.¹ It is well-established that T2-weighted (T2w) magnetic resonance imaging (MRI) provides improved CaP detection and localization compared to transrectal ultrasound.² Dynamic-contrast enhanced (DCE) MRI, which is useful for analyzing tumor angiogenesis, has been shown to facilitate improved CaP detection accuracy compared to T2w MRI alone.³⁻⁶ On DCE MRI CaP regions manifest rapid and increased enhancement and early washout compared to surrounding normal prostate tissue.⁷ Quantitative pharmacokinetic (PK) analysis of DCE MRI provides for the determination of parameters, such as K^{trans} (transfer constant) and v_e (extravascular-extracellular volume fraction), that describe tumor vasculature perfusion and permeability.⁸ These constants are known to be elevated in CaP and are relevant for CaP detection and prognosis.⁹ Furthermore, because microvessel density is correlated with Gleason grades, PK parameters may be beneficial for assessing CaP aggressiveness.¹⁰

Send correspondence to A.M.: anant.madabhushi@case.edu.

This work was made possible by grants from the National Institute of Health (R01CA136535, R01CA140772, R43EB015199, R21CA167811), National Science Foundation (IIP-1248316), the QED award from the University City Science Center and Rutgers University, and the National Science Foundation Graduate Research Fellowship.

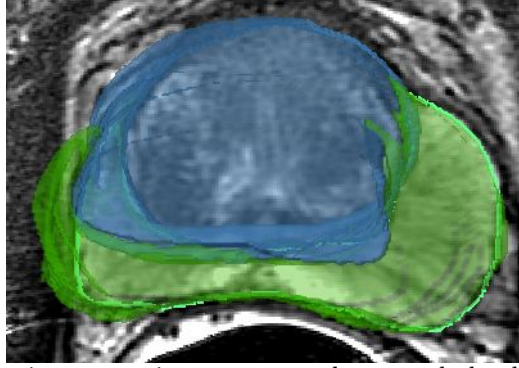


Figure 1: The prostate gland contains two main structures: the central gland shown in blue and the peripheral zone shown in green.

Recent studies have shown that the appearance of CaP on T2w MRI varies based on the spatial location of CaP in the prostate.⁷ The prostate gland can be divided into two primary anatomical regions (see Figure 1): the outer peripheral zone (PZ), and the central gland (CG), comprised of both the inner central and the transitional zones. Seventy percent of prostate tumors occur in the PZ, where they appear as regions of low signal intensity surrounded by brighter normal PZ tissue.^{7,8} Most of the remaining prostate tumors are found in the CG, where they manifest as homogeneous, lenticular-shaped lesions with low signal intensity.^{7,8} It is notable that PZ tumors tend to be more aggressive than CG tumors.¹¹ Furthermore, it was recently shown that CG CaP and PZ CaP possess distinct quantitative imaging signatures on multi-protocol MRI.³² While a number of studies have determined PK parameter values in CaP and surrounding benign prostate regions,^{12–16} we are not aware of any study that investigated variations in PK constants based on the manifestation of CaP in either the CG or the PZ. Since PK parameter values are associated with CaP grade,¹⁰ investigating variations in PK parameter values based on the spatial location of cancerous lesions in the prostate gland may lead to improved understanding, characterization and prognostication of CaP. The first objective of this study is to leverage PK modeling to calculate PK constants both for CG CaP and for PZ CaP and to determine whether PK parameter values are significantly different depending on the spatial location of CaP in the prostate gland.

There are a number of techniques to estimate PK parameter values, many of which require knowledge of the time-resolved concentration of the contrast agent (CA) in the blood plasma, the arterial input function (AIF). Nevertheless, when no artery is present in the image field-of-view, estimating the AIF is unfeasible. The multiple reference tissue method (MRTM) enables the estimation of PK parameters without the AIF by leveraging PK parameter values from the literature for a reference tissue in the field-of-view. However, MRTM relies on population-averaged PK constants for the reference tissue, ignoring inter-patient variation. In an effort to obtain more accurate patient-specific PK parameter values, we introduce iterative MRTM (IMRTM) to leverage MRTM to estimate PK constants while avoiding reliance on assumptions about the PK constants associated with a reference tissue. This is accomplished by iteratively cycling among the tissues for which PK parameter values will be estimated and invoking MRTM to update the PK parameter values associated with each tissue until the PK parameter values no longer change. The novelty of IMRTM lies in its ability to estimate patient-specific PK parameters that do not depend on the accuracy of population-averaged values. Additionally, IMRTM facilitates PK analysis when the field-of-view does not contain a suitable artery or a reference tissue that is well-characterized in the literature. Nevertheless, because it is difficult to validate our findings in the absence of an AIF, more validation of IMRTM must be done using simulated DCE MRI data.

The remainder of this paper is organized as follows. In Section 2 we review published methods for performing PK modeling on prostate DCE MRI. We review the theory behind the MRTM and IMRTM techniques in Section 3. In Section 4 we describe our experimental methods for evaluating IMRTM on 15 prostate DCE MRI studies to estimate PK parameters for normal CG, normal PZ, and CaP. We discuss our PK analysis results, comparing MRTM and IMRTM, in Section 5, and in Section 6 we provide some concluding remarks.

2. PREVIOUS WORK

PK analysis of CaP on DCE MRI requires a PK model that relates signal intensities on DCE MRI to the underlying physiology. The two-compartment Kety–Tofts model²⁰ assumes that a low molecular weight CA diffuses from the vascular space into the extravascular–extracellular space and then slowly leaks back in the vascular space. The rate of forward transfer, K^{trans} , and the extravascular–extracellular volume fraction, v_e , can be estimated from this model, which requires knowledge of the concentration of the CA in the blood plasma, or the AIF, to measure these PK constants.

The most accurate technique for determining the AIF involves introducing a catheter into the subject’s artery and sampling blood at intervals during the image acquisition process.²¹ The drawbacks of this method include both its invasiveness and the low temporal resolution of the acquired DCE MRI data.¹⁷ A second technique avoids the invasive nature of this procedure by averaging the AIFs measured in a small cohort of patients via the first technique and then assuming that this average AIF is valid for all subsequent patients.²² The advantage of this method is that a population-averaged AIF can be “lifted” from published literature and then applied to all experimental subjects without the need for direct measurement of the AIF. Unfortunately, this method ignores both intra- and inter-subject variations in the AIF that may lead to errors in PK analysis if they are not accounted for.²³ A third technique leverages an artery in the image field-of-view to simultaneously assess enhancement in both the blood and the tissue and uses this information to accurately determine the AIF.²⁴ While this method provides an accurate measurement of the AIF on a patient-specific basis, this approach requires high temporal resolution, attained at the expense of lowering the spatial resolution.¹⁷ Especially in the analysis of tumors, the need for high spatial resolution and the fact that a suitable artery may not be present in the field-of-view are major limitations to its use.

Because of the challenges associated with measuring the AIF, several studies have circumvented the AIF in performing PK analysis. These studies fall into two general categories: model-based blind estimation techniques and reference-region approaches.^{17, 18, 25–28} The blind estimation method leverages tissue concentration curves in a portion of the image to estimate the AIF, which is constrained to a particular functional form.^{25–27} Unfortunately, these methods involve highly parameterized functions that are time-consuming to optimize. Furthermore, the need for an independently-determined AIF scale factor is another substantial drawback since inaccuracies in the scaling of the AIF may bias PK parameter estimates.²⁷

In addition to blind AIF estimation approaches, the multiple reference tissue method (MRTM)^{17, 28} was introduced to circumvent the AIF in estimating PK parameter values. This method leverages a reference tissue with well-characterized PK parameter values, such as skeletal muscle, to estimate PK parameter values for a tumor. Nevertheless, the MRTM requires accurate knowledge of the K^{trans} and v_e values for a reference tissue. Because PK parameters vary between subjects even for well-characterized reference tissues,¹⁸ literature values for K^{trans} and v_e of the reference tissue may introduce error into PK parameter estimation for the tumor. To avoid reliance on PK parameter values from the literature, Lee et al.¹⁸ introduced a modified MRTM that estimates relative K^{trans} and v_e values, which was applied for PK modeling in the brain. Nevertheless, this method relies on a literature value for K^{trans} of the reference tissue. Although K^{trans} measured in the brain may not vary significantly between patients, the range of PK parameter values estimated within the prostate gland varies greatly between studies.^{12, 14, 16} Consequently, assuming that population-averaged PK parameter values for the CG and PZ apply to all patients is not advantageous. Rather, a technique to estimate PK parameters in the prostate that does not rely on assumed values from the literature would have considerable value.

3. THEORY

3.1 Notation

We define an MR image scene as $\mathcal{D} = (d, S)$, where each voxel d in the MR image is associated with a T -dimensional vector S containing the DCE MRI intensity values obtained at the T time points. Each $d \in \mathcal{D}$ is also associated with a label $y \in \{0, 1\}$, where $y(d) = 0$ if voxel d is benign and $y(d) = 1$ otherwise. Define the complementary sets $\mathcal{D}_A = \{d : y(d) = 0\}$ and $\mathcal{D}_B = \{d : y(d) = 1\}$ with cardinalities n_A and n_B , respectively.

3.2 Multiple Reference Tissue Method

The MRTM^{17,18,28} assumes a simple two-compartment model in which the CA diffuses from the blood plasma into the extravascular-extracellular spaces of multiple tissues. When only two distinct tissues are considered, this system can be described by two differential equations:

$$\frac{d}{dt}C^A(t) = K^A C^p(t) - \frac{K^A}{v^A} C^A(t) \quad (1)$$

$$\frac{d}{dt}C^B(t) = K^B C^p(t) - \frac{K^B}{v^B} C^B(t) \quad (2)$$

where $C^p(t)$ is the concentration of CA in the blood plasma, also known as the AIF; $C^A(t)$ and $C^B(t)$ are the concentrations of CA in tissues A and B ; K^A and K^B are the transfer constants representing diffusion of CA from capillaries into tissues A and B ; and v^A and v^B are the extravascular-extracellular volume fractions for tissues A and B , respectively. Combining equations (1) and (2) into a single equation eliminates the dependence on $C^p(t)$:

$$\frac{d}{dt}C^B(t) + \frac{K^B}{v^B} C^B(t) = \frac{K^B}{K^A} \frac{d}{dt}C^A(t) + \frac{K^B}{v^A} C^A(t). \quad (3)$$

The solution to this differential equation can be expressed as

$$C^A(t) = \frac{K^B}{K^A} C^B(t) + \frac{K^B}{K^A} \left(\frac{K^B}{v^B} - \frac{K^A}{v^A} \right) \int_0^T C^B(t) e^{-\frac{K^A}{v^A}(T-t)} dt \quad (4)$$

or

$$C^B(t) = \frac{K^A}{K^B} C^A(t) + \frac{K^A}{K^B} \left(\frac{K^A}{v^A} - \frac{K^B}{v^B} \right) \int_0^T C^A(t) e^{-\frac{K^B}{v^B}(T-t)} dt. \quad (5)$$

Thus, assuming that $C^A(t)$ and $C^B(t)$ can be measured and that K^B and v^B are known, equation (4) can be implemented in a curve-fitting routine to estimate values for K^A and v^A . Similarly, assuming that K^A and v^A are known, equation (5) can be implemented in a curve-fitting routine to estimate values for K^B and v^B .

3.3 Iterative Multiple Reference Tissue Method

IMRTM involves iteratively implementing MRTM to solve for the PK parameters of each reference tissue until the PK parameters no longer change. At every iteration, MRTM is applied to estimate PK constants on a per-pixel basis, and the mean PK parameter values for each tissue are taken as the new PK parameter values. Assuming that initial values for K^A and v^A are known, equation (5) is used to estimate values for $K^B(d)$ and $v^B(d) \forall d \in \mathcal{D}_B$. Once pixel-wise values for $K^B(d)$ and $v^B(d)$ have been estimated, tissue-specific values for K^B and v^B are obtained via maximum likelihood estimation. The joint distribution of $(K^B(d), v^B(d))$ is approximately bivariate Gaussian with mean $\mu = (\mu_K, \mu_v)$, variance $\sigma = (\sigma_K, \sigma_v)$, and correlation ρ :

$$f(K, v) = \frac{\exp\left(-\frac{1}{2(1-\rho^2)} \left[\frac{(K-\mu_K)^2}{\sigma_K^2} + \frac{(v-\mu_v)^2}{\sigma_v^2} - \frac{2\rho(K-\mu_K)(v-\mu_v)}{\sigma_K \sigma_v} \right]\right)}{2\pi\sigma_K\sigma_v\sqrt{1-\rho^2}} \quad (6)$$

The maximum likelihood estimators (MLEs) for μ_K and μ_v can be computed as $\bar{\mu}_K = \sum_{d \in \mathcal{D}_B} \frac{K^B(d)}{n_B}$ and $\bar{\mu}_v = \sum_{d \in \mathcal{D}_B} \frac{v^B(d)}{n_B}$. Assigning $K^B = \bar{\mu}_K$ and $v^B = \bar{\mu}_v$ facilitates the estimation of $K^A(d)$ and $v^A(d) \forall d \in \mathcal{D}_A$ using equation (4). Finally, assuming that $(K^A(d), v^A(d))$ are jointly normally distributed facilitates the re-estimation of $K^A = \sum_{d \in \mathcal{D}_A} \frac{K^A(d)}{n_A}$ and $v^A = \sum_{d \in \mathcal{D}_A} \frac{v^A(d)}{n_A}$, the MLEs of $f(K^A, v^A)$. This cycle is repeated—re-estimating K^B and v^B on a pixel-wise basis and obtaining the MLEs in order to re-estimate K^A and v^A on a

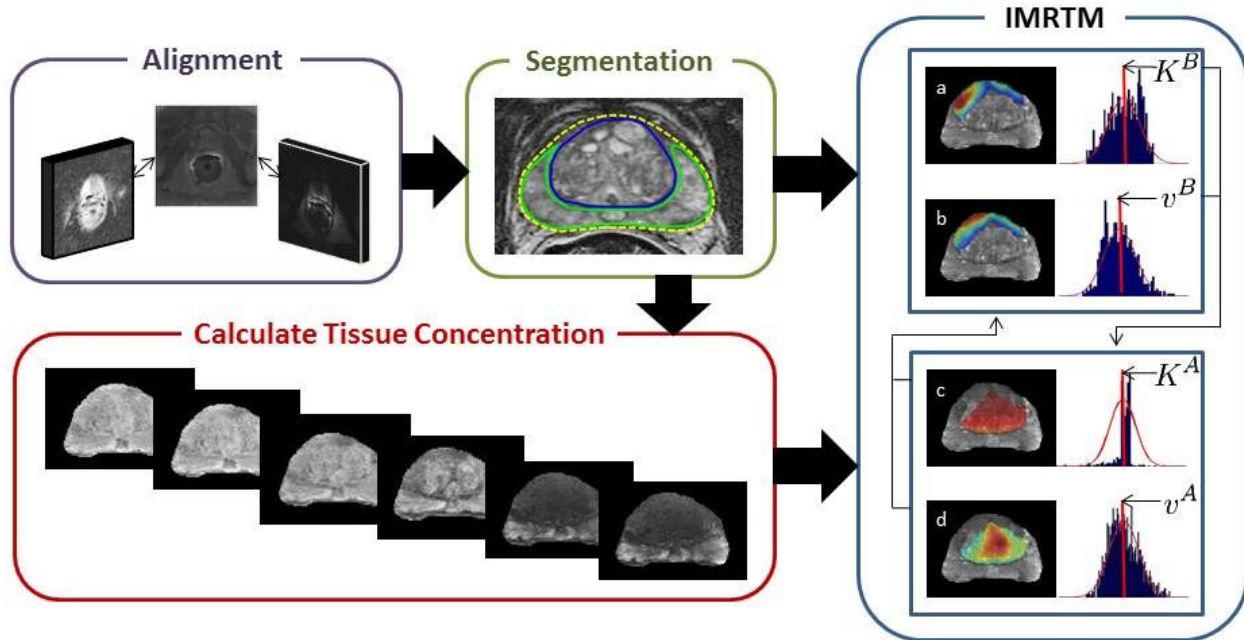


Figure 2: Flowchart of IMRTM methodology: First multi-protocol MR images are aligned; the prostate gland, as well as the CG and PZ, are segmented on T2w MRI; and CA concentration in the prostate is computed. Then, IMRTM is performed as follows. Given starting values for K^A and v^A , pixel-wise maps of K^B (a) and v^B (b) are obtained. Normal curves are fit to the histograms, and K^B and v^B , taken as the MLEs, are used to estimate pixel-wise maps of K^A (c) and v^A (d). Once again, normal curves are fit to these histograms and updated values of K^A and v^A are taken as the MLEs. These values are then used in the next iteration to update K^B and v^B , and so on.

pixel-wise basis—until the values no longer change for either tissue. Thus, IMRTM cycles between updating PK parameter values for tissues A and B until the PK parameter values converge for both regions. A summary of IMRTM is illustrated in Figure 2, and the IMRTM algorithm is detailed in Algorithm 1.

4. EXPERIMENTAL DESIGN

4.1 Description of Data

A total of 15 pre-operative, endorectal *in vivo* 3 Tesla MR imaging studies including T2w, DWI, and DCE MRI in men with organ-confined CaP were obtained prior to radical prostatectomy at the Beth Israel Deaconess Medical Center. The DCE MRI protocol included two pre-contrast images, which were acquired at 95 second intervals before the bolus injection of 0.1 mmol/kg of gadolinium-DTPA, and five post-contrast images that were acquired subsequently at the same temporal resolution. The DCE MRI parameters were TR = 9.3 ms, TE = 4.2 ms, and flip angle = 18°. Following radical prostatectomy, the excised glands were sectioned and stained with hematoxylin and eosin (H&E), attempting to ensure at all times that the sectioning was done in a plane corresponding to the preoperative MRI.

4.2 Registration of MRI and WMHS slices

In order to obtain ground truth annotation of CaP extent on *in vivo* MRI, multi-modal registration of MRI and WMHS was performed. A pathologist and radiologist working in unison visually identified 55 corresponding 2D whole-mount histological sections (WMHS) and axial MRI slices from the 15 studies. These correspondences were established by means of anatomical fiducials such as the urethra, verumontanum, and prominent nodules of benign prostatic hyperplasia that were visually discernible on both histology and preoperative MRI.²⁹ The

Algorithm 1 IMRTM()

Input: Maps of CA concentration in the tissue, obtained from DCE MR image with tissues A and B in the field-of-view. Initial values for K^A , K^B , v^A , and v^B . Tolerance value ϵ and large value Δ .

Output: Final values for K^A , K^B , v^A , and v^B .

- 1: Let $i = 0$, $K_1^A = K^A$ and $v_1^A = v^A$.
 - 2: **if** $\Delta > \epsilon$ **then**
 - 3: Let $i = i + 1$.
 - 4: **for all** $d \in \mathcal{D}_B$ **do**
 - 5: Use K_i^A and v_i^A and equation (5) to estimate $K^B(d)$ and $v^B(d)$.
 - 6: **end for**
 - 7: Compute $K^B = \bar{\mu}_K$ and $v^B = \bar{\mu}_v$.
 - 8: **for all** $d \in \mathcal{D}_A$ **do**
 - 9: Use K_i^B and v_i^B and equation (4) to estimate $K^A(d)$ and $v^A(d)$.
 - 10: **end for**
 - 11: Compute $K^A = \bar{\mu}_K$ and $v^A = \bar{\mu}_v$.
 - 12: Let $\Delta = \max\{|K_i^A - K_{i-1}^A|, |K_i^B - K_{i-1}^B|, |v_i^A - v_{i-1}^A|, |v_i^B - v_{i-1}^B|\}$.
 - 13: **end if**
-

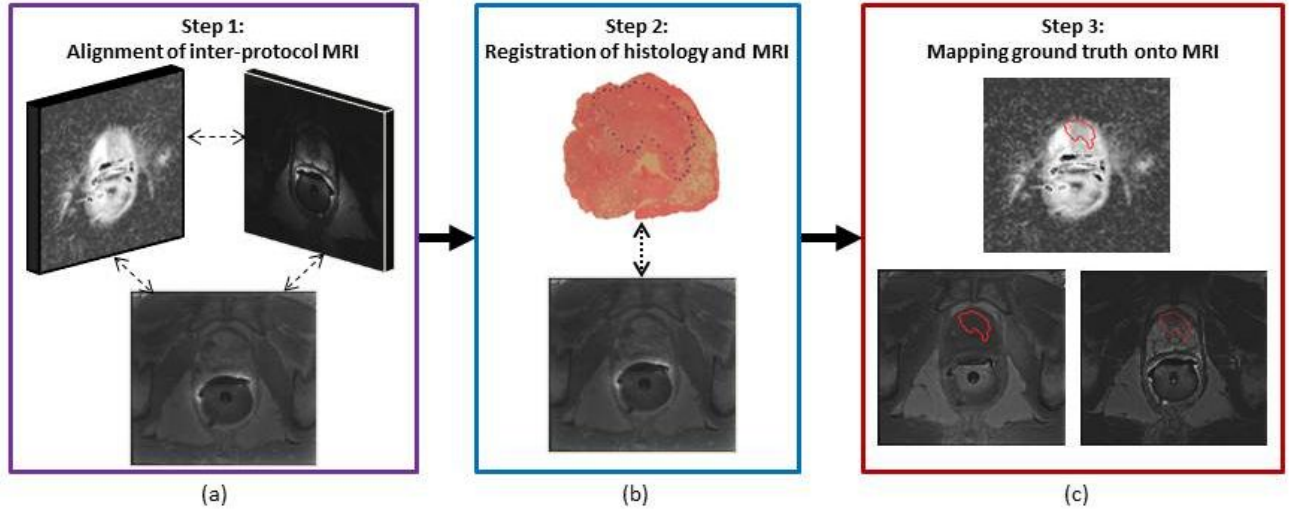


Figure 3: Flowchart of registration technique: (a) First T2w, DWI, and DCE MRI are aligned, and then (b) MRI is registered with histology so that (c) ground truth extent of CaP can be mapped from histology onto MRI.

following steps were performed in order to align all 55 corresponding 2D WMHS slices with T2w, DWI, and DCE MRI and subsequently map spatial extent of CaP from histology onto MRI (see Figure 3).

4.2.1 Step 1: Alignment of Inter-Protocol MRI

First T2w MRI and ADC maps obtained from DWI were brought into spatial alignment with DCE MRI via volumetric affine registration, which corrected for inter-acquisition movement and resolution differences between the MRI protocols.³⁰ Slice correspondences between T2w, DCE, and ADC images, as well as relative voxel locations and sizes, were determined using stored DICOM image header information.

4.2.2 Step 2: Registration of Histology and MRI

Once T2w, DCE, and ADC images were brought into spatial alignment, multi-modal registration of *in vivo* MRI with *ex vivo* WMHS was performed. Registration of WMHS and MRI is complicated both by differences in image intensities and nonlinear differences in the shape of the prostate due to the presence of an endorectal coil

during MR imaging and deformations to the histological section upon fixation and sectioning.^{29,30} Consequently, achieving correct alignment of such images requires elastic transformations to overcome the nonlinear shape differences. However, driving such transformations by means of traditional intensity-based similarity measures, such as mutual information (MI), is usually suboptimal for robustly registering dissimilar modalities.³¹ We therefore use a nonrigid registration scheme³⁰ driven by a higher-order variant of MI that handles images with very different intensities (e.g., MRI and WMHS data) and deformation characteristics (e.g., *in vivo* to *ex vivo*). The spatial alignment of the two modalities is implemented in two steps. First an initial affine alignment of WMHS to the corresponding T2w MRI slice is done. This enables correction of large translations, rotations, and differences in image scale. Then, automated nonrigid registration of the rigidly aligned WMHS and T2w MRI is performed by means of a fully automated nonlinear hierarchical (multiscale) B-spline mesh grid image warping scheme.³⁰

4.2.3 Step 3: Mapping Ground Truth onto MRI

Spatial extent of CaP was mapped from WMHS slices onto the corresponding MP MRI slices. The spatial extent of CaP mapped onto MRI was examined and manually corrected (as required) by an expert radiologist using Photoshop (Adobe Systems Inc., CA). The final result of this procedure was a labeling of each DCE MRI voxel within the prostate as corresponding to CaP or non-CaP prostate tissue.

4.3 Prostate Segmentation

Viswanath et al.³² and others³³ have demonstrated that CG and PZ CaP have different appearances on T2w MRI and do not share the same quantitative imaging signatures on MRI.³² Furthermore, PK parameter values have been shown to vary significantly between different regions of the prostate.^{12,14,16} A secondary goal of this study was to evaluate whether the PK parameter values estimated using IMRTM are significantly different for CG CaP and PZ CaP. Consequently, the CG and PZ were manually segmented on T2w MRI by a radiologist, and each patient study was classified as having CG or PZ CaP if more than 70% of the tumor volume was found to be present in a particular zone, based on the recommendations of McNeal.¹⁹ Of the 15 data sets, nine were thus determined as having PZ CaP, while the remaining six were identified as having CaP in the CG. To ensure that the sets of CG and PZ CaP were as distinct from each other as possible, only sections displaying an explicit focus of CaP in either the CG or the PZ were included in this analysis.

4.4 Calculation of Tissue Concentration

Assuming the fast exchange limit and that both repetition time (TR) and echo time (TE) are small, the relationship between the CA concentration $C(t)$ and the native T_1 value can be estimated well by the following approximation:

$$C(t) \approx \frac{S(t) - S(0)}{r_1 T_1(0) S(0)}, \quad (7)$$

where $S(t)$ represents the DCE-MRI signal for a particular voxel at time t and r_1 is the relaxivity constant.³⁴ Thus, $C(t)$ can be estimated for each voxel by leveraging literature values for the native T_1 values and assuming that $r_1 = 3.7 \text{ s}^{-1} \text{ mM}^{-1}$ for 3 Tesla MRI.³⁵ Several researchers have shown that native T_1 values range between 1350 and 1670 ms for different prostate regions,^{16,36,38} but T_1 values are not significantly different between highly glandular-ductal tissues and stromal-low ductal tissues,^{36,38} nor between normal and cancerous prostate tissue.³⁷ Consequently, we assumed that a native T_1 value of 1520 ms applied both to normal CG and PZ and to cancerous regions. It is important to note that varying native T_1 values was found to have little impact on subsequent PK modeling.³⁸

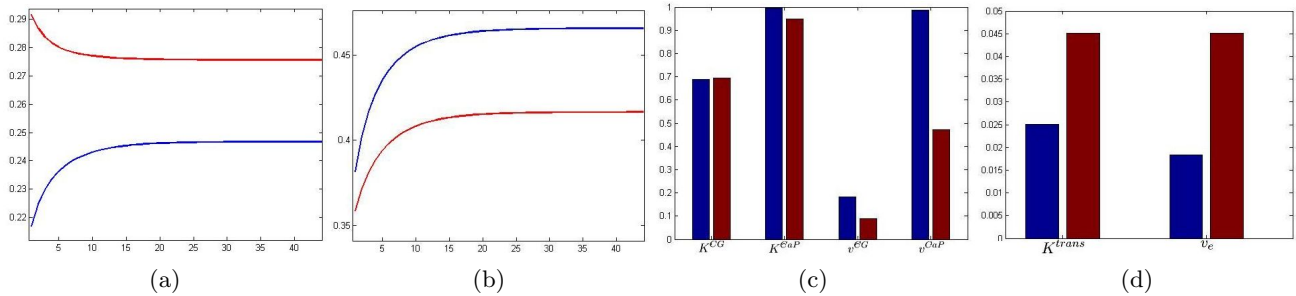


Figure 4: Plots of (a) K^{trans} and (b) v_e as they evolve during the iterations of IMRTM are shown for a representative study containing CG CaP. The correlations between the initial and final PK parameter values are shown in (c) for MRTM in blue and IMRTM in red, and p -values obtained in a Kruskal-Wallis one-way analysis of variance test comparing the means of PK parameters estimated in CG and PZ CaP are plotted in (d) for MRTM in blue and IMRTM in red.

4.5 Estimation of Pharmacokinetic Parameters

In order to confirm that PK constants returned by IMRTM are reasonable and to evaluate the benefits of IMRTM for PK parameter estimation, we compared PK constants obtained via MRTM with those obtained via IMRTM. Toward this end, regions-of-interest (ROIs) 9×9 pixels in size were selected in both normal and cancerous prostate tissue. For the six studies that contain CaP in the CG, the selected ROIs were fully contained in the CG; conversely, for the nine studies with CaP in the PZ, both selected ROIs were fully contained in the PZ. PK parameters K^{trans} and v_e were estimated for each pair of normal and cancerous ROIs as follows. For studies containing CG CaP, the ROI selected in the normal region of the CG was used to model tissue A while the ROI manifesting CG CaP modeled tissue B , and K^{CG} , K_{CG}^{CaP} , v^{CG} , and v_{CG}^{CaP} were estimated via both MRTM and IMRTM. Similarly, for studies containing CaP in the PZ, the ROI selected in the normal region of the PZ was used to model tissue A while the ROI manifesting PZ CaP modeled tissue B , and K^{PZ} , K_{PZ}^{CaP} , v^{PZ} , and v_{PZ}^{CaP} were estimated via both MRTM and IMRTM.

$C^A(t)$ and $C^B(t)$ were calculated using equation (7), and PK parameter values from previous studies^{12,14,16} were used to initialize K^A and v^A , the PK parameters associated with normal prostate tissue. Starting values for K^A were 0.26 and 0.22 for normal CG and normal PZ, respectively, and for v^A were 0.38 and 0.32 for normal CG and normal PZ, respectively.¹² PK parameter values for K^{trans} and v_e were estimated using Algorithm 1. This resulted in PK parameter values for each individual voxel, as well as general values for tissues A and B , the benign and malignant regions of the prostate.

Once PK constants were estimated for each 9×9 -pixel ROI via both MRTM and IMRTM, the parameters resulting from the MRTM and IMRTM algorithms are used in conjunction with equations (4) and (5) to estimate PK parameter values on a per-pixel basis for each pixel in the CG or PZ (depending on the location of CaP in the prostate gland for each study). Maps of K^{trans} and v_e throughout the CG or PZ were obtained in this way and used for qualitative comparison of MRTM and IMRTM.

4.6 Evaluation of Sensitivity to Initial Parameters

In order to evaluate the sensitivity of the PK parameters estimated via IMRTM to starting values obtained from population-averaged studies, we varied initial values for the PK constants to determine the effect on the resulting PK parameter values. Starting values for K^A and K^B were made to vary between .15 and .3, while initial v^A and v^B values were made to vary from .3 to .5. A single pair of 9×9 -pixel ROIs selected in a study containing CG CaP, as well as another pair of 9×9 -pixel ROIs selected in a study with PZ CaP, was selected for this task. The correlations between the initial and final PK parameter values for both MRTM and IMRTM were obtained.

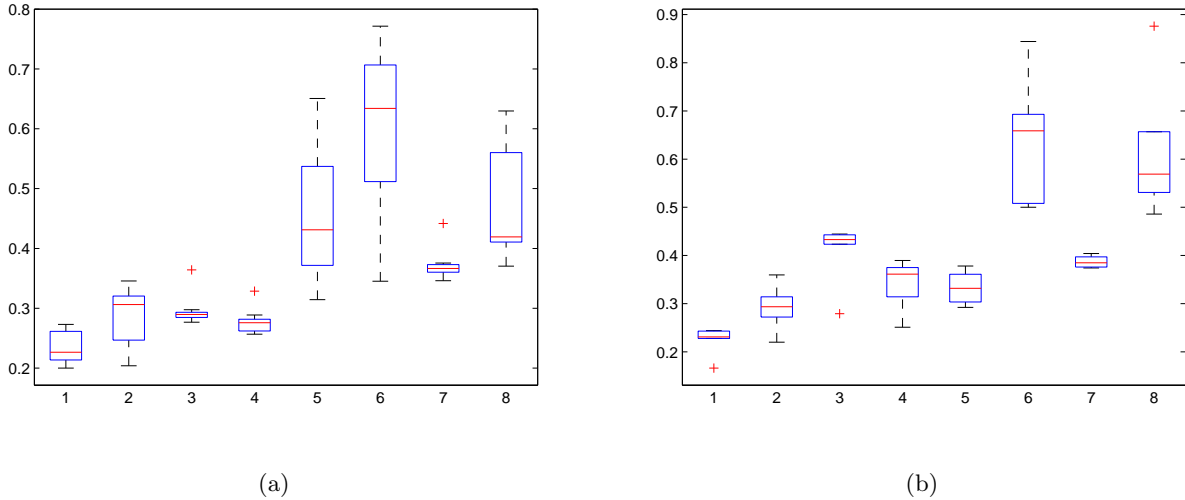


Figure 5: Boxplots of the estimated values for K^{trans} and v_e are shown for (a) the six studies with CG CaP and (b) the nine studies with CaP located in the PZ. Columns 1 and 2 represent K^{trans} estimated in normal CG tissue for MRTM and IMRTM, respectively; columns 3 and 4 represent K^{trans} estimated in CaP regions for MRTM and IMRTM, respectively; columns 5 and 6 represent v_e estimated in normal CG tissue for MRTM and IMRTM, respectively; and columns 7 and 8 represent v_e estimated in CaP regions for MRTM and IMRTM, respectively.

5. EXPERIMENTAL RESULTS AND DISCUSSION

5.1 Comparison of MRTM and IMRTM

Plots illustrating the evolution of the PK parameters during the iterations of IMRTM are displayed in Figures 4a-b for a representative study containing CaP in the CG. PK parameter values obtained at iteration 1 of IMRTM are equivalent to PK parameter values obtained via MRTM. Clearly, when permitted to evolve for multiple iterations, PK constants move away from their MRTM values towards patient-specific values. Resulting PK parameter estimates obtained via MRTM and IMRTM, summarized in Figure 5, are within the range of biologically feasible values.¹² Values for the PK parameters K^{trans} and v_e estimated via IMRTM average 0.29 and 0.60 for normal CG, 0.29 and 0.64 for normal PZ, and 0.30 and 0.53 for CaP. Whereas K^{trans} values estimated by IMRTM are well-within the range of previously reported values,^{12,14,16} v_e values estimated by IMRTM tend to be higher than values reported in the literature. It is noteworthy that the range of estimated PK parameter values is substantially greater for IMRTM than for MRTM, probably because there is less bias from population-averaged values. Maps of K^{trans} and v_e are shown in Figure 6 for a study containing CG CaP and a study with PZ CaP. Note that for these cases K^{trans} is a more sensitive indicator of CaP in the CG when it is estimated via IMRTM than when it is obtained using MRTM, whereas v_e maps do not differ substantively between the two methods.

5.2 Sensitivity of IMRTM to Initial Parameters

Initial values for the PK constants were varied to determine the effect on the resulting PK parameter values. Boxplots of the estimated values for K^{trans} and v_e are displayed in Figure 7. Because MRTM relies heavily on population-averaged starting values for the PK constants, varying these starting values leads to a large range of PK constants; in contrast, IMRTM is less sensitive to variation in population-averaged PK constants. The correlations between the initial and final PK parameter values for both MRTM and IMRTM are shown in Figure 4c. While K^{trans} is relatively robust to variation of the initial PK parameter values, v_e is more sensitive to initial values. This finding corroborates the notion that less inter-patient variation occurs in K^{trans} than in v_e ¹⁸ but suggests that allowing the PK constants to evolve enables the PK parameters to move away from the initial values, towards patient-specific values.

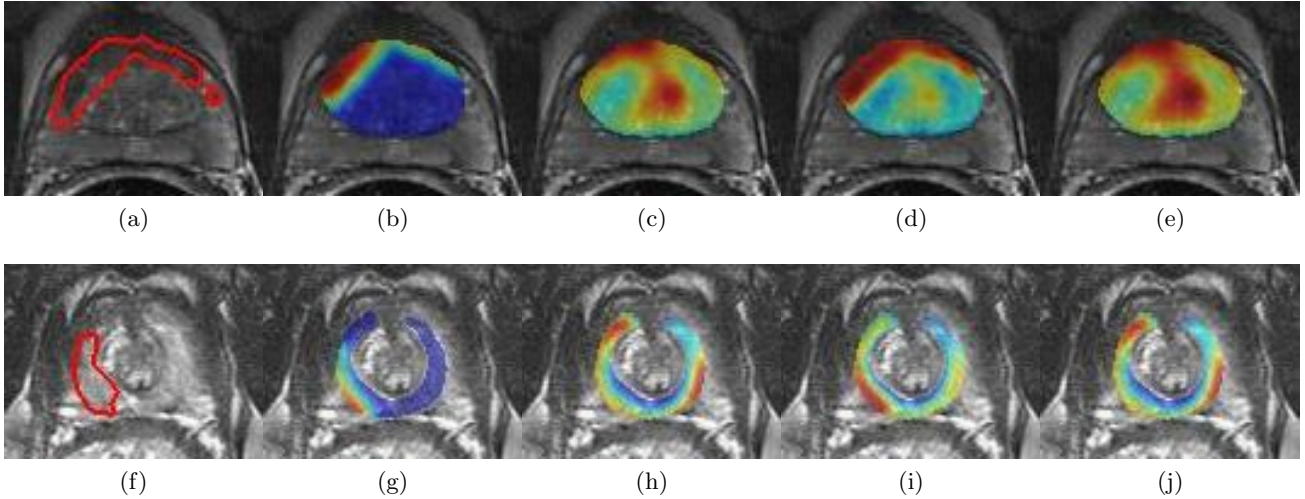


Figure 6: Ground truth extent of CaP is shown for a representative slice of a CG tumor (a) and PZ tumor (b). Maps of K^{trans} and v_e are displayed in (b), (g) and (c), (h) for MRTM and in (d), (i) and (e), (j) for IMRTM, respectively.

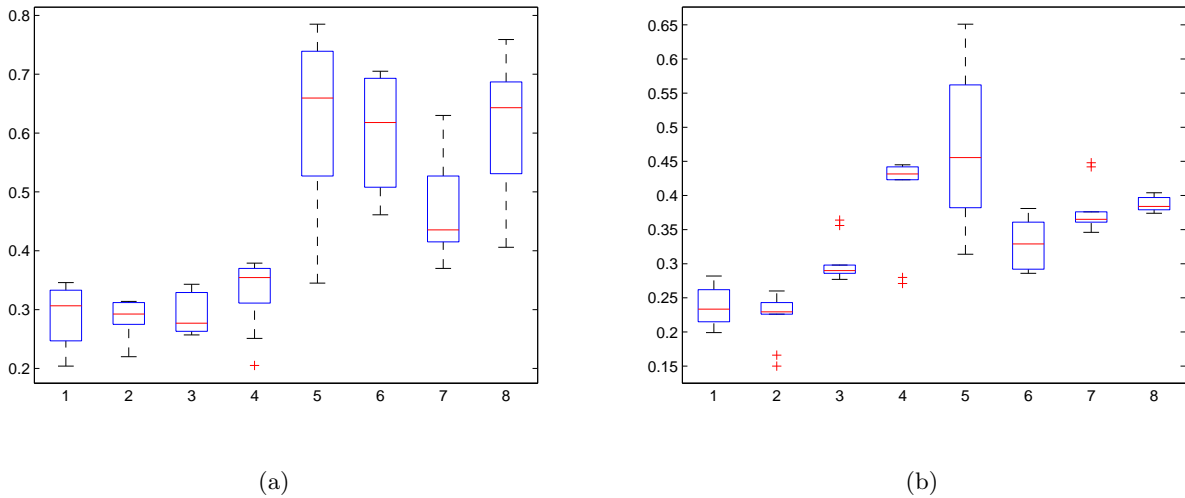


Figure 7: Boxplots of the estimated values for K^{trans} and v_e when initial PK constants were varied are shown for (a) MRTM and (b) IMRTM. Columns 1 and 2 represent K^{trans} estimated in normal CG and normal PZ, respectively; columns 3 and 4 represent K^{trans} estimated in CG CaP and PZ CaP, respectively; columns 5 and 6 represent v_e estimated in normal CG and normal PZ, respectively; and columns 7 and 8 represent v_e estimated in CG CaP and PZ CaP, respectively.

5.3 Differences Between CG and PZ CaP

Differences between PK constants estimated in CG and PZ tumors were assessed using Kruskal–Wallis one-way analysis of variance (see Figure 4d). Independent of the method, both the transfer rate constants and the extravascular–extracellular volume fractions associated with CG tumors were significantly lower than in PZ tumors ($p < 0.05$). This finding suggests that CG and PZ tumors do not share the same perfusion characteristics. In light of the facts that PZ CaP tends to be more aggressive than CG CaP¹¹ and PK constants are increased in more aggressive CaP,¹⁰ our result makes sense intuitively.

6. CONCLUDING REMARKS

The objectives of this study were (a) to eliminate the need to rely on population-averaged PK constants of a reference tissue when utilizing the MRTM to estimate PK constants for tumors and (b) to investigate whether PK constants differ between CG and PZ CaP. We presented a novel method for estimating PK constants on DCE MRI without relying on PK parameter values for a reference tissue. IMRTM can be implemented for PK analysis in other organs in addition to prostate and is easily generalizable to estimate PK parameter values for multiple regions or tissues by iteratively estimating PK parameter values in more than two reference tissues. When we applied our iterative method in the context of CaP characterization we found that PK constants associated with PZ CaP are significantly higher than those associated with CG CaP. Since PZ tumors tend to be more aggressive than their CG counterparts and PK constants are expected to increase with cancer aggressiveness, this result is not surprising. The fact that PK constants vary significantly between CG CaP and PZ CaP, as well as between normal CG and PZ, suggests that both accurate segmentation of the prostate into CG and PZ and correct delineation of the anatomical region of the prostate containing the tumor focus are useful and necessary first steps for PK modeling of CaP. Although further corroboration on a larger cohort of patients is needed, this initial finding points to the importance of accurately segmenting prostate regions prior to the application of PK models to estimate perfusion characteristics of CaP regions.

This study had a few limitations. Firstly, in the absence of the true AIF it is difficult to validate our findings; we can only compare the PK parameter values we obtained with those previously reported in the literature. Although the values obtained via IMRTM for v_e are higher than expected, they are within the range of biological feasibility, and the values obtained for K^{trans} are similar to those reported in previous studies.^{12,14,16} Nevertheless, in order to better validate our findings, we intend to simulate DCE MRI data using a parameterized form of the AIF with known PK parameter values and evaluate the performance of IMRTM in recovering these PK constants. Secondly, because of tumor heterogeneity, PK parameter values may vary even within a single tumor. Hence, our analysis of small regions of normal and malignant prostate tissue may not accurately represent the entire prostate gland or tumor. Finally, since a larger study is necessary to confirm pharmacokinetic differences in CG CaP and PZ CaP, in the future we plan to expand our analysis to include a larger cohort of patients that would provide sufficient statistical power for this end.

REFERENCES

- [1] Kohler, B.A., Ward, E., McCarthy, B.J., et al. Annual report to the nation on the status of cancer, 1975-2007, featuring tumors of the brain and other nervous system. *Journal of the National Cancer Institute* **103**, 1-23 (2011).
- [2] Chabanova, E., Balslev, I., Logager, V., et al. Prostate cancer: 1.5 T endo-coil dynamic contrast-enhanced MRI and MR spectroscopy—correlation with prostate biopsy and prostatectomy histopathological data. *European Journal of Radiology* **80**, 292-6 (2011).
- [3] Jager, G.J., Ruijter, E.T., van de Kaa, C.A. Dynamic TurboFLASH subtraction technique for contrast-enhanced MR imaging of the prostate: correlation with histopathologic results. *Radiology* **203**, 645-52 (1997).
- [4] Futterer, J.J., Heijmink, S.W., Scheenen, T.W., et al. Prostate cancer localization with dynamic contrast-enhanced MR imaging and proton MR spectroscopic imaging. *Radiology* **241**, 449-58 (2006).
- [5] Delongchamps, N.B., Rouanne, M., Flam, T., et al. Multiparametric magnetic resonance imaging for the detection and localization of prostate cancer: combination of T2-weighted, dynamic contrast-enhanced and diffusion-weighted imaging. *British Journal of Urology International* **107**, 1411-8 (2011).
- [6] Hara, N., Okuizumi, Bilim, V., et al. Dynamic contrast-enhanced magnetic resonance imaging (DCE-MRI) is a useful modality for the precise detection and staging of early prostate cancer. *Prostate* **62**(1), 140-7 (2005).
- [7] Turkbey, B., Bernardo, M., Merino, M.J., et al. MRI of localized prostate cancer: coming of age in the PSA era. *Diagnostic Interventional Radiology* **18**, 34-45 (2012).
- [8] Futterer, J.J. and Barentsz, J.O. 3T MRI of prostate cancer. *Applied Radiology* **38**, 25-32 (2009).
- [9] Alonzi, R., Padhani, A.R., Allen, C. Dynamic contrast enhanced MRI in prostate cancer. *European Journal of Radiology* **63**, 335-50 (2007).

- [10] Sinha, A.A., Quast, B.J., Reddy, P.K., et al. Microvessel density as a molecular marker for identifying high-grade prostatic intraepithelial neoplasia precursors to prostate cancer. *Experimental and Molecular Pathology* **77**, 153-9 (2004).
- [11] Shannon, B.A., McNeal, J.E., Cohen, R.J. Transition zone carcinoma of the prostate gland: a common indolent tumour type that occasionally manifests aggressive behaviour. *Pathology* **35**, 467-71 (2003).
- [12] Jackson, A.S.N., Reinsberg, Dearnaley, D.P., et al. Dynamic contrast-enhanced MRI for prostate cancer localization. *The British Journal of Radiology* **82**, 148-56 (2009).
- [13] van Dorsten, F.A., van der Graaf, M., Engelbrecht, M.R., et al. Combined quantitative dynamic contrast-enhanced MR imaging and (1)H MR spectroscopic imaging of human prostate cancer. *Journal of Magnetic Resonance Imaging* **20**, 279-87 (2004).
- [14] Ocak, I., Bernardo, M., Choyke, P.L., et al. Dynamic contrast-enhanced MRI of prostate cancer at 3T: A study of pharmacokinetic parameters. *American Journal of Roentgenology* **189**(4), W192-201 (2007).
- [15] Riches, S.F., Payne, G.S., Morgan, V.A., et al. MRI in the detection of prostate cancer: combined apparent diffusion coefficient, metabolite ratio, and vascular parameters. *American Journal of Roentgenology* **193**, 1583-91 (2009).
- [16] Lowry, M., Zelhof, B., Turnbull, L.W., et al. Analysis of prostate DCE-MRI: Comparison of fast exchange limit and fast exchange regimen pharmacokinetic models in the discrimination of malignant from normal tissue. *Investigative Radiology* **44**(9), 577-84 (2009).
- [17] Yankeelov, T.E., Luci, J.J., Gore, J.C., et al. Quantitative pharmacokinetic analysis of DCE-MRI data without an arterial input function: A reference region model. *Magnetic Resonance Imaging* **23**, 519-29 (2005).
- [18] Lee, J., Platt, S., Zhao, Q., et al. An analysis of the pharmacokinetic parameter ratios in DCE-MRI using a reference region model. *Magnetic Resonance Imaging* **30**, 26-35 (2012).
- [19] McNeal, J.E. Regional morphology and pathology of the prostate. *American Journal of Clinical Pathology* **49**, 347-57 (1968).
- [20] Tofts, P.S., Brix, G., Buckley, D.L., et al. Estimating kinetic parameters from dynamic contrast-enhanced T(1)-weighted MRI of a diffusable tracer: standardized quantities and symbols. *Journal of Magnetic Resonance Imaging* **10**, 223-32 (1999).
- [21] Fritz-Hansen, T., Rostrup, E., Larsson, H.B.W., et al. Measurement of the arterial concentration of Gd-DTPA using MRI: a step toward quantitative perfusion imaging. *Magnetic Resonance in Medicine* **16**, 117-31 (1996).
- [22] Meng, R., Chang, S.D., Jones, E.C., et al. Comparison between population average and experimentally measured arterial input function in predicting biopsy results in prostate cancer. *Academic Radiology* **17**, 520-5 (2010).
- [23] Simpson, N.E., He, Z., Evelhoch, J.L. Deuterium NMR tissue perfusion measurements using the tracer uptake approach: I. Optimization of methods. *Magnetic Resonance in Medicine* **42**, 42-52 (1999).
- [24] Port, R.E., Knopp, M.V., Hoffmann, U., et al. Multicompartment analysis of gadolinium chelate kinetics: blood-tissue exchange in mammary tumors as monitored by dynamic MR imaging. *Journal of Magnetic Resonance Imaging* **10**, 233-41 (1999).
- [25] Riabkov, D.Y., DiBella, E.V.R. Estimation of kinetic parameters without input functions: analysis of three methods for multichannel blind estimation. *IEEE Transactions on Biomedical Engineering* **49**, 1318-27 (2002).
- [26] Fluckiger, J.U., Schabel, M.C., DiBella, E.V.R. Model-based blind estimation of kinetic parameters in dynamic contrast enhanced (DCE)-MRI. *Magnetic Resonance in Medicine* **62**, 1477-86 (2009).
- [27] Schabel, M.C., Fluckiger, J.U., DiBella, E.V.R. A model-constrained Monte Carlo method for blind arterial input function estimation in dynamic contrast-enhanced MRI: I. Simulations. *Physics in Medicine and Biology* **55**, 4783-806 (2010).
- [28] Yang, C., Karczmar, G.S., Medved, M., et al. Estimating the arterial input function using two reference tissues in dynamic contrast-enhanced MRI studies: fundamental concepts and simulations. *Magnetic Resonance in Medicine* **52**, 1110-7 (2004).
- [29] Xiao, G., Bloch, B.N., Chappelow, J., et al. Determining histology-MRI slice correspondences for defining MRI-based disease signatures of prostate cancer. *Computerized Medical Imaging and Graphics* **35** 568-578 (2011).

- [30] Chappelow, J., Boch, B.N., Madabhushi, A., et al. Elastic registration of multimodal prostate MRI and histology via multiattribute combined mutual information. *Medical Physics* **38**, 2005-18 (2011).
- [31] Pluim, J.P., Maintz, J.B., and Viergever, M.A. Image registration by maximization of combined mutual information and gradient information. *IEEE Transactions on Medical Imaging* **19** 809-14 (2000).
- [32] Viswanath, S.E., Bloch, N.B., Chappelow, J.C., et al. Central gland and peripheral zone prostate tumors have significantly different quantitative imaging signatures on 3 Tesla endorectal, in vivo T2-weighted MR imagery. *Journal of Magnetic Resonance Imaging* **36** 213-24 (2012).
- [33] Akin, O., Sala, E., Moskowitz, C.S., et al. Transition zone prostate cancers: features, detection, localization, and staging at endorectal MR imaging. *Radiology* **239** 784-92 (2006).
- [34] Medved, M., Karczmar, G., Stadler, W.M., et al. Semiquantitative analysis of dynamic contrast enhanced MRI in cancer patients: variability and changes in tumor tissue over time. *Journal of Magnetic Resonance Imaging* **20**, 122-8 (2004).
- [35] Rohrer, M., Baurer, H., Mintorovitch, J., et al. Comparison of magnetic properties of MRI contrast media solutions at different magnetic field strengths. *Investigative Radiology* **40**, 715-724 (2005).
- [36] Noworolski, S.M., Henry, R.G., Vigneron, D.B., et al. Dynamic contrast-enhanced MRI in normal and abnormal prostate tissues as defined by biopsy, MRI, and 3D MRSI. *Magnetic Resonance in Medicine* **53**, 249-55 (2005).
- [37] Buckley, D.L., Roberts, C., Parker, G.J., et al. Prostate cancer: evaluation of vascular characteristics with dynamic contrast-enhanced T1-weighted MR imaging—initial experience. *Radiology* **233**, 709-15 (2004).
- [38] Noworolski, S.M., Vigneron, D.B., Chen, A.P., et al. Combined dynamic contrast-enhanced MRI and MR diffusion imaging to distinguish between glandular and stromal prostatic tissues. *Magnetic Resonance Imaging* **26**, 1071-80 (2008).